

Instabilities driven by diffusio-phoretic flow on catalytic surfaces

Yibo Chen¹, Kai Leong Chong^{1,†}, Luoqin Liu¹, Roberto Verzicco^{1,2,3}
and Detlef Lohse^{1,4,‡}

¹Physics of Fluids Group, Max Planck Center for Complex Fluid Dynamics, MESA+ Institute and J.M.Burgers Center for Fluid Dynamics, University of Twente, P.O. Box 217, 7500 AE Enschede, The Netherlands

²Dipartimento di Ingegneria Industriale, University of Rome ‘Tor Vergata’, Via del Politecnico 1, Roma 00133, Italy

³Gran Sasso Science Institute - Viale F. Crispi, 7 67100 L’Aquila, Italy

⁴Max Planck Institute for Dynamics and Self-Organisation, 37077 Göttingen, Germany

(Received xx; revised xx; accepted xx)

We theoretically and numerically investigate the instabilities driven by diffusio-phoretic flow, caused by a solutal concentration gradient along a reacting surface. The important control parameter is the Péclet number Pe , which quantifies the ratio of the solutal advection rate to the diffusion rate. First, we study the diffusio-phoretic flow on a catalytic plane in two dimensions. From a linear stability analysis, we obtain that for Pe larger than 8π , mass transport by convection overtakes that by diffusion, and a symmetry-breaking mode arises, which is consistent with numerical results. For even larger Pe , non-linear terms become important. For $Pe > 16\pi$, multiple concentration plumes are emitted from the catalytic plane, which eventually merge into a single larger one. When Pe is even larger ($Pe \gtrsim 603$ for Schmidt number $Sc = 1$), there are continuous emissions and merging events of the concentration plumes. This newly-found flow state reflects the non-linear saturation of the system. The critical Péclet number for the transition to this state depends on Schmidt number Sc . In the second part of the paper, we conduct three-dimensional simulations for spherical catalytic particles, and beyond a critical Péclet number again find continuous plume emission and plume merging, now leading to a chaotic motion of the phoretic particle. Our results thus help to understand the experimentally observed chaotic motion of catalytic particles in the high Pe regime.

Key words:

1. Introduction

Self-propulsion at the micrometer scale frequently occurs in nature (Lauga & Thomas 2009; Lauga 2016; Bray 2000; Jeanneret *et al.* 2016). For example, micro-organisms self-propel to search for nutrients, different temperatures, or sunlight. Inspired by such motile biological organisms, extensive studies on artificial micro-swimmers have been done over the last one and a half decades, especially on self-propelled phoretic particles (Jiang *et al.* 2010; Moran & Posner 2017; Golestanian *et al.* 2007; Qi *et al.* 2020; Maass *et al.*

† Email address for correspondence: k.l.chong@utwente.nl

‡ Email address for correspondence: d.lohse@utwente.nl

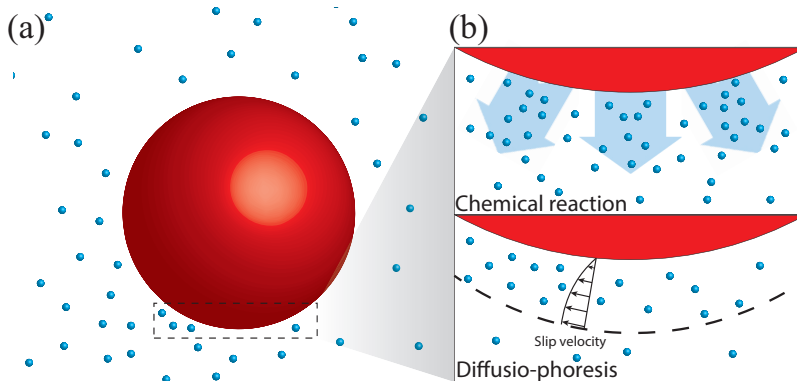


FIGURE 1. Schematic illustration of the catalytic particles (red) with chemical reaction and diffusio-phoresis near the interface. The product originating from the catalytic reaction at the particle surface is shown in cyan. (b) shows a zoom-in of (a). If there is a concentration gradient at the interface, a slip velocity is induced (diffusio-phoresis). Beyond a critical reaction rate (expressed as a critical Péclet number), such gradient emerges through a linear instability.

2016; Bär *et al.* 2020; Jin *et al.* 2017). Also dissolving or chemically reacting droplets can show such phenomena (Krüger *et al.* 2016; Li *et al.* 2019; Vajdi Hokmabad *et al.* 2019; Lohse & Zhang 2020). A typical feature of the self-propelled particles is that, instead of swimming with appendages, they can propel themselves by converting free energy from the environment into kinetic energy (Ramaswamy 2010; Ebbens & Howse 2010).

The driving mechanism behind the propulsion of phoretic particles is diffusio-phoresis (Anderson 1989). Note that in some literature the terminology “diffusio-osmotic effect” is used to indicate the same mechanism. The basic feature is that whenever there exists a tangential concentration gradient on the surface of the particle, there is an induced flow within the interaction layer adjacent to the surface, as shown in figure 1. Since the layer is much thinner than the size of the object, the flow is conveniently described with a slip velocity at the surface (Golestanian *et al.* 2007). This effect can also be generalized to other coupled fields such as the temperature or the electric fields. The resulting flows are respectively referred to as thermo-phoretic or electro-phoretic (Piazza 2008; Squires & Bazant 2006; Long *et al.* 1999; Moran & Posner 2011).

The classical mathematical framework for the study of self-propelled particles has often neglected the effect of solute advection (Golestanian *et al.* 2007). The previous work by Michelin *et al.* (2013), however, has revealed that the Péclet number Pe is an important parameter controlling the motion of self-propelled particles. Pe is the ratio of the solute advection to the diffusion rates. Through a linear stability analysis and corresponding simulations, Michelin *et al.* (2013) found that when Pe is larger than the critical value $Pe_{cr} = 4$, a spherical active particle by dissolution and chemical reaction exhibits a motion in a preferred direction which breaks the rotational symmetry of the system. Later, Michelin & Lauga (2014) performed a comprehensive theoretical study on how the moving speed of the active particle depends on Pe , and generalized the theory to any coverage of the reacting surface.

For large enough Pe , some fascinating features can emerge. Hu *et al.* (2019) have numerically observed that for large enough Péclet numbers, such an active isotropic particle acquires chaotic trajectories. Analogously, in the problem of active droplets, Ruckenstein (1981) also found similar helical or chaotic motions, as caused by the interfacial Marangoni flow (Suga *et al.* 2018; Maass *et al.* 2016; Herminghaus *et al.* 2014).

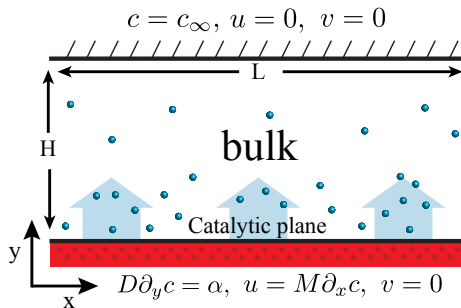


FIGURE 2. The setup of the system with the boundary conditions. A wall is at the top and a catalytic plane is located at the bottom. Periodic boundary conditions are applied in x-direction.

Though the phenomena of active droplets and active particles look similar, Krüger *et al.* (2016) explained that the helical trajectory of the active droplet is attributed to the coupling between the internal flow and the direction of the nematic field, whereas such internal flow is obviously absent in particles. In a further study, Morozov & Michelin (2019) have considered both Marangoni and diffusio-phoretic effects into their numerical simulation, and also demonstrate that a chaotic oscillation of the droplet can occur.

Motivated by the above recent findings, in this paper we focus on the instability due to chemical reactions and the resulting diffusio-phoretic flow near a catalytic interface, especially in the large Pe regime. To start with some reduced complexity, we first consider a simplified model, namely diffusio-phoretic flow over a catalytic plane, in order to study the dynamics near the catalytic surface (see figure 2). This simplified model can reproduce the important features of the diffusio-phoretic flow, and it is also convenient to avoid the added complexities arising from the curvature of the surface. Note that recently Michelin *et al.* (2020) also studied such a simplified model. Building on their work, in the present study we further demonstrate the existence of a new regime with continuous plume emission and merging. In the second part of the paper we go beyond the simplified model and numerically examine the plume emission and merging phenomena for chaotically-moving phoretic particles.

The paper is organized as follows: After a description of the problem setup and the control parameters in Section 2, the linear stability analysis for the catalytic plane system is performed in Section 3. Then the numerical method and numerical setup are provided in Section 4.1. The numerical results for the catalytic plane are presented in Section 4.2. Then we extend our research to phoretic particle in Section 5. Finally, conclusions and outlook to further work are given in Section 6.

2. Problem setup and control parameters

We start with the two-dimensional system sketched in figure 2. A fluid layer is confined by a solid wall on the top and a catalytic plane at the bottom, with periodic boundary conditions on both sides. The width and the height of the domain are denoted by L and H , respectively. The physical variables to describe the system are the concentration of the product $\hat{c}(x, y, t)$ and the velocity of the fluid $\hat{\mathbf{u}}(x, y, t)$. Note that all dimensional physical variables are marked with hat (e.g. \hat{c} , $\hat{\mathbf{u}}$), while the dimensionless ones without (e.g. c , \mathbf{u}). At the catalytic surface, chemical reactions take place which convert the reactant into the product. By assuming a constant reaction rate, the concentration boundary condition

of the product at the bottom plane is given by

$$D \frac{\partial \hat{c}}{\partial \hat{y}} = \alpha, \quad (2.1)$$

where D is the diffusivity of the product in the fluid and α measures the strength of the reaction activity at the catalytic surface, i.e. the generation of solute by the reaction.

The tangential concentration gradient induces a slip velocity at the surface of the plane. This is the so-called diffusio-phoretic flow, which is parallel to the surface and its magnitude is proportional to the tangential concentration gradient. The relationship between the induced slip velocity and the tangential concentration gradient is thus given by

$$\hat{u}(y=0) = M \frac{\partial \hat{c}}{\partial \hat{x}}, \quad (2.2)$$

where M is the phoretic mobility. The sign of M can either be positive or negative, depending on the type of the solute-surface interaction (Anderson 1989). Michelin *et al.* (2013) prove that the diffusio-phoretic system is unstable only if $M\alpha$ is positive. In this work, we study the case $M > 0$ and $\alpha > 0$.

The time evolution of the concentration field $c(x, y, t)$ and the velocity field $\mathbf{u}(x, y, t) = (u(x, y, t), v(x, y, t))$ are governed by the Navier-Stokes equation and the convection-diffusion equation. The characteristic scales for non-dimensionalization are $M\alpha/D$ for velocities, L for lengths and $\alpha L/D$ for concentrations. The dimensionless form of the governing equations can then be written as:

$$\frac{\partial c}{\partial t} + \mathbf{u} \cdot \nabla c = \frac{1}{Pe} \nabla^2 c, \quad (2.3)$$

$$\frac{\partial \mathbf{u}}{\partial t} + (\mathbf{u} \cdot \nabla) \mathbf{u} = -\nabla p + \frac{Sc}{Pe} \nabla^2 \mathbf{u}, \quad \nabla \cdot \mathbf{u} = 0, \quad (2.4a, b)$$

where Pe is the Péclet number, characterizing the strengths of the driving and Sc the Schmidt number, characterizing the ratio between the momentum and mass diffusivities:

$$Pe = \frac{M\alpha L}{D^2}, \quad Sc = \frac{\nu}{D}. \quad (2.5a, b)$$

In dimensionless form, the concentration boundary condition at the catalytic plane becomes

$$\left. \frac{\partial c}{\partial y} \right|_{y=0} = A, \quad (2.6)$$

where $A = \alpha/\alpha = 1$ is the dimensionless emission rate. The tangential velocity is proportional to the tangential concentration gradient, and its dimensionless form is

$$u|_{y=0} = \frac{\partial c}{\partial x}, \quad (2.7)$$

while the normal component of the velocity vanishes at the plane surface

$$v|_{y=0} = 0. \quad (2.8)$$

Both the velocity and the concentration boundary conditions at the top wall are zero,

$$\mathbf{u}|_{y=H} = 0, \quad c|_{y=H} = 0. \quad (2.9a, b)$$

3. Linear stability analysis for catalytic plane

In this section, the linear stability analysis is performed to investigate the stability of the system. [Michelin *et al.* \(2020\)](#) presented similar findings in the limit $Sc \rightarrow \infty$ (Stokes flow), here we generalize their result to general Sc .

In the linear stability analysis we add small amplitude perturbations to the reference steady state:

$$\mathbf{u} = \bar{\mathbf{u}}(x, y) + \epsilon \tilde{\mathbf{u}}(x, y, t), \quad p = \bar{p}(x, y) + \epsilon \tilde{p}(x, y, t), \quad c = \bar{c}(x, y) + \epsilon \tilde{c}(x, y, t), \quad (3.1)$$

where $\bar{\mathbf{u}}$, \bar{p} and \bar{c} are the basic state of the velocity, pressure and concentration fields, and $\epsilon \tilde{\mathbf{u}}$, $\epsilon \tilde{p}$ and $\epsilon \tilde{c}$ are small perturbations with the coefficient $\epsilon \ll 1$.

A trivial solution to the basic configuration is a static state with fully developed diffusion. Substitute zero velocity into (2.3), the time evolution of the concentration field is ([Wu *et al.* 2006](#))

$$c(y, t) = \int_0^t \frac{-A}{\sqrt{\pi Pe(t-\tau)}} \exp\left[-\frac{Pe y^2}{4(t-\tau)}\right] d\tau. \quad (3.2)$$

For $t \rightarrow \infty$, we obtain a spatially constant concentration gradient,

$$\frac{\partial c(y, t)}{\partial y} = A. \quad (3.3)$$

Substituting equations (3.1) and (3.3) into the governing equations (2.3) and (2.4), with static basic flow $\bar{\mathbf{u}}(x, y) = 0$, the linearized governing equations are:

$$\frac{\partial \tilde{c}}{\partial t} = -\tilde{v}A + \frac{1}{Pe} \nabla^2 \tilde{c}, \quad (3.4)$$

$$\frac{\partial \tilde{\mathbf{u}}}{\partial t} = -\nabla \tilde{p} + \frac{Sc}{Pe} \nabla^2 \tilde{\mathbf{u}}, \quad \nabla \cdot \tilde{\mathbf{u}} = 0. \quad (3.5a, b)$$

We now assume as ansatz a separation of variables and periodic behavior in lateral direction,

$$(\tilde{u}(x, y, t), \tilde{v}(x, y, t), \tilde{p}(x, y, t), \tilde{c}(x, y, t)) = (u_0(y), v_0(y), p_0(y), c_0(y)) e^{ikx+st}, \quad (3.6)$$

where $k = 2\pi n$ and $n \in \mathbb{N}$ is the wavenumber. The sign of the exponential growth rate s determines whether the system is stable.

Combining the above equations (3.4)-(3.6) and the boundary conditions, we obtain the relation which allows us to analytically calculate how the stability depends on Pe and Sc (detailed derivations are in Supplementary Materials):

$$Pe = k \sqrt{1 + \frac{sPe}{k^2}} \left(1 + \sqrt{1 + \frac{sPe}{k^2}} \right) \left(\sqrt{1 + \frac{sPe}{Sc k^2}} + \sqrt{1 + \frac{sPe}{k^2}} \right). \quad (3.7)$$

From this implicit equation we can calculate the exponential growth rate s for any parameters of Pe and Sc . The sign of s determines the flow stability of the system: $s > 0$ means exponential growth, or instability (the larger, the more unstable), whereas $s < 0$ indicates stability.

Assuming $s = 0$ in equation (3.7), we get the critical Pe for transition from stability to instability for different wavenumber n ,

$$Pe_{cr} = 4k = 8\pi n. \quad (3.8)$$

Note that Pe_{cr} is independent of Sc .

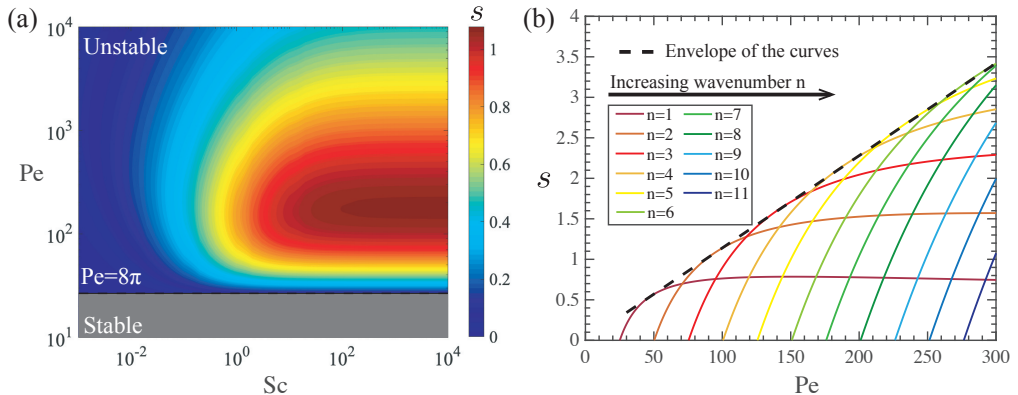


FIGURE 3. (a) Stability diagram for the catalytic plane in the Pe vs Sc parameter space for wavenumber $n = 1$. An eigenvalue $s > 0$ indicates instability. The color represents the actual value of s , i.e., the strength of the exponential growth. When $Pe > 8\pi$, s is positive and the system is unstable, independently of Sc . (b) s as a function of Pe at various wavenumber for $Sc = 1$ by linear stability analysis. The wavenumber of the curve increases from left to right. For wavenumber n , when $Pe < 8\pi n$, s is negative and the system is stable. When $Pe > 8\pi n$, s becomes positive and the system becomes unstable towards this mode n . The function of the envelope of the curves (dashed line in (b)) is equation (3.9).

If we combine equation (3.7) and its derivative with respect to n , we obtain the function of the envelope of the curves at different wavenumber for $Sc = 1$:

$$s = \frac{85\sqrt{17} - 349}{128} Pe \approx 0.0114Pe. \quad (3.9)$$

The dominant wavenumber for a certain Pe and $Sc = 1$ is (for a detailed derivation see the Supplementary material):

$$n_{max} = \frac{31 - 7\sqrt{17}}{32\pi} Pe \approx 0.0213Pe. \quad (3.10)$$

The exponential growth rate s as obtained from equation (3.7) as function of Pe and Sc for the case of $n = 1$ is shown in figure 3(a). As we see from this analytical result, the system is unstable for $Pe > 8\pi$. Moreover, s as a function of Pe for different wavenumbers and $Sc = 1$ is plotted by the solid curves in figure 3(b). The dashed line shows the envelope of the curves, which is equation (3.9)

The linearized diffusion-convection equation (3.4) helps us to understand the physical mechanism of the diffusio-phoretic instability. If there is local concentration variation at the surface, the diffusion term $\frac{1}{Pe} \nabla^2 c$ smoothes out the local concentration difference, which makes the system stable. In contrast, dominance of the advection term $-u \cdot \nabla c$ will increase the concentration difference, such that the system becomes unstable. Thus it can be seen that the competing mass transport by diffusion and advection determines the instability, which is quantified by Pe . If Pe is above a critical value, the advection term results in positive feedback, which amplifies the disturbance and leads to the instability.

4. Simulation of catalytic plane

We now numerically study the diffusio-osmotic instability. The objective of the numerical simulation is to understand the effect of the non-linear terms and random initial perturbation which obviously are ignored in the linear stability analysis.

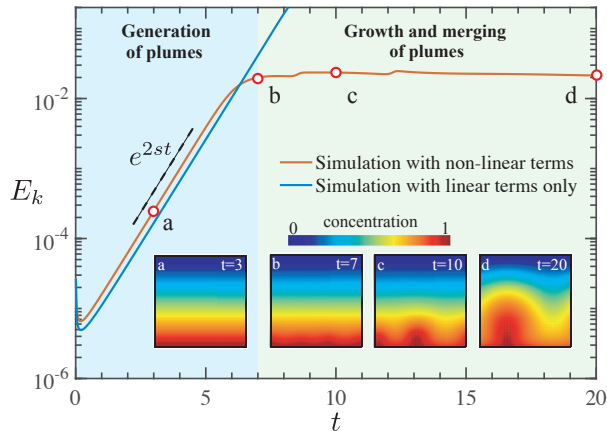


FIGURE 4. Time evolution of the kinetic energy E_k for the case $Pe = 125$ and $Sc = 1$ with random perturbation from simulations with only linear terms (blue solid curve) and with both linear and non-linear terms (red solid curve). The kinetic energy E_k is in log scale. For the case with both linear and non-linear terms, the growth of E_k levels off near time instant b, compared to that with only linear terms, because of non-linear saturation. The process is divided into two subprocesses: plume generation and plume growth and merging. During the first subprocess, E_k grows exponentially $E_k \sim e^{2st}$. The points at the curve represents four states in the process, of which the concentration fields are shown in panels a to d, respectively. (a) Plume generating: Triggered by a perturbation, the kinetic energy increases exponentially. (b-d) Plume growing and merging. As E_k reaches around 0.02, the kinetic energy reaches a plateau; at the same time the plumes emerge in the concentration field. The plumes grow and merge with each other. In the end, only one major plume remains in the field (d).

4.1. Numerical setups

The fluid motion and concentration field are solved using direct numerical simulation (DNS) of the Navier-Stokes equations and diffusion-convection equation in Cartesian coordinates. Equations (2.3)-(2.4) are spatially discretized using the central second-order finite difference scheme. Along both horizontal and vertical directions, homogenous staggered grids are used. The equations are integrated by a fractional-step method with the nonlinear terms computed explicitly by a low-storage third-order Runge Kutta scheme and the viscous terms computed implicitly by a Crank-Nicolson scheme (Verzicco & Orlandi 1996; van der Poel *et al.* 2015). The simulations are then conducted with the concentration and the velocity boundary conditions written in equations (2.6)-(2.9). We have inspected the finite domain size effect, and found that if the aspect ratio of the system $H/L \geq 0.9$, the growth rate of the instability becomes insensitive to the aspect ratio. Thus for all the simulations, the aspect ratio 1 has been chosen, and the mesh 401×401 has been used.

The initial condition is the fluid at rest and a constant concentration gradient along the y-direction (see equation (3.3)). Then a small sinusoidal perturbation is added to the concentration field to trigger the instability:

$$\delta c = 10^{-4} \sin(2\pi n x), \quad (4.1)$$

where n is the wavenumber of the perturbation.

4.2. Nonlinear saturation

To quantify the long term growth of the instability, we examine how the kinetic energy E_k , averaged over the entire domain, changes in time. An example time series of E_k is

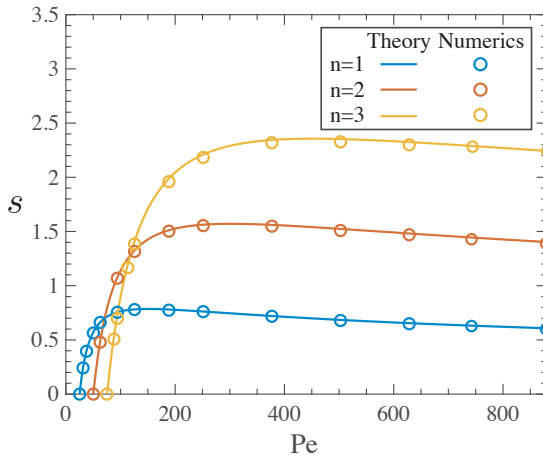


FIGURE 5. Theoretical (solid lines) and numerical results (circles) of exponential growth rate s for different wavenumber $n = 1, 2, 3$ and $Sc = 1$. The simulations are performed with only linear terms.

shown in figure 4, which corresponds to the case of $Sc = 1$ and $Pe = 125$. The result suggests that after the initial perturbation, there is a transient stage during which the kinetic energy grows exponentially, i.e. $E_k \sim e^{2st}$. As a consistency test, our simulation confirms that the involvement of non-linear terms in the simulation does not change the initial exponential growth rate s . However, later the growth of E_k begins to level off after some time because of non-linear saturation. Such non-linear saturation is common in most linearly unstable non-linear systems, such as Rayleigh-Bénard convection (Greenside & Coughran Jr 1984), Taylor-Couette flow for inner cylinder rotation (Grossmann *et al.* 2016), or Rayleigh-Taylor instability (Haan 1989). The concentration fields at different time instants show that during the saturated stage, the emitted plumes merge into a larger one, and eventually the flow structure develops into the state with a single large plume.

Next, we compare the exponential growth rate s of the instability for various wavenumber cases ($n = 1, 2, 3$) during the initial stage with exponential growth as shown in figure 5. For the benchmark cases with only the linear terms, the data points (circles) agree excellently with the linear stability analysis (solid curves). This result can be regarded as further validation for our numerical code.

We further examine the situation with random initial perturbation solved with the full equation, including nonlinear terms. The above theoretical analysis are shown that for higher Pe , the larger wavenumber mode can be triggered. The concentration fields in figure 6(a) provide more insight into the triggering of higher-order modes for larger Pe . Different time instants of the concentration fields for different Pe are shown in the figure. For $Pe = 50$, there is a single concentration plume generating initially. However, for larger $Pe = 125$, multiple plumes are initially emitted. They undergo a merging process to form a single large plume. After formation of the single large plume, E_k reaches the asymptotic value shown in the time series in figure 6(b). Interestingly, for even larger $Pe = 628$, E_k has spiky signals within a statistically steady state as shown in figure 6(c). The corresponding concentration fields in figure 6(a) reveals that small plumes are continuously generated from the reacting wall, and the merging of the plumes occurs

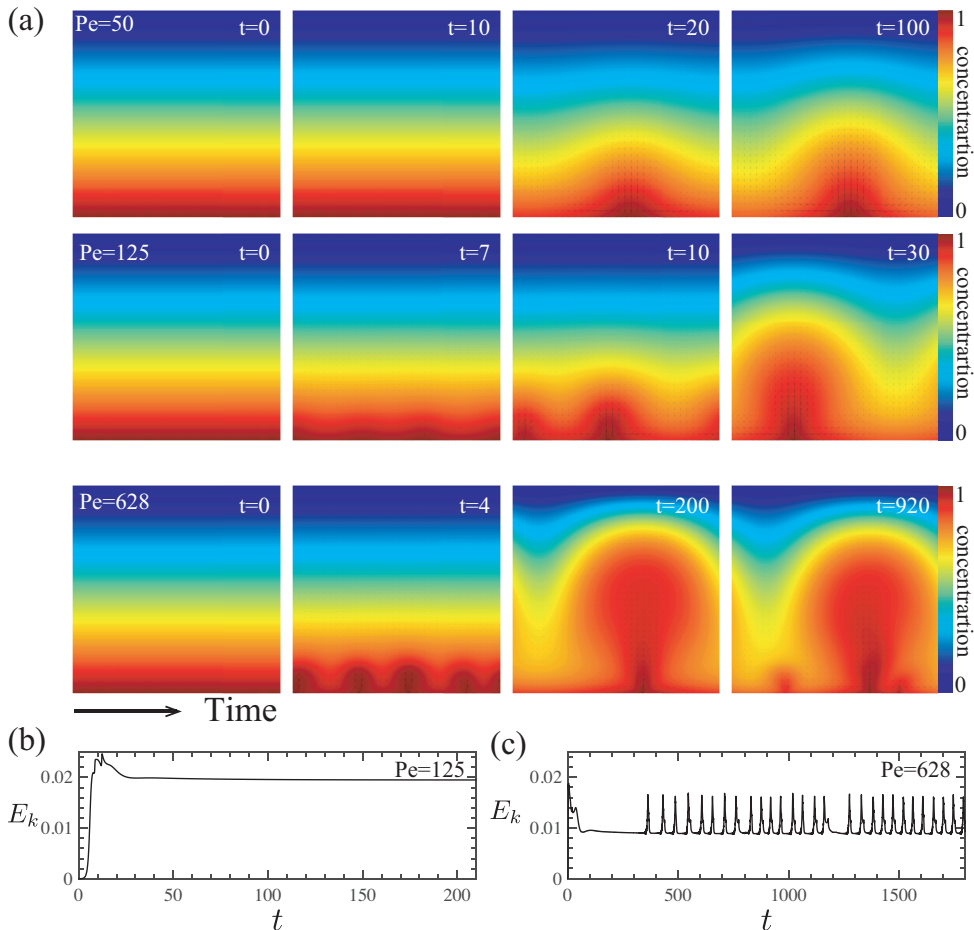


FIGURE 6. (a) The concentration contours for different Pe numbers: $Pe = 50$, $Pe = 125$, and $Pe = 628$. The simulations are based on random initial perturbation and performed with the full equations, including the non-linear terms. Four snapshots in time are plotted for each Pe . First column: beginning state; second and third column: intermediate states; final column: final (statistical) stable state. (b-c) Time evolution of the total kinetic energy of the velocity field for $Pe = 125$ (b) and 628 (c). For the case of $Pe = 125$, the kinetic energy in the final stage converges, while for $Pe = 628$ it shows spiky and intermittent signals.

simultaneously. Such continuous plume emission and merging can also clearly be seen from the Supplementary Movie.

Finally, we classify the four regimes based on the three criteria:

- Growth rate of the instability.
- Number of plumes generated initially.
- Fluctuation of the kinetic energy (E_k) after reaching the statistical steady state.

To quantify the number of generated plumes in the initial stage, we perform a Fourier transformation of the concentration along the reacting wall ($y = 0$) at the point when the E_k reaches a constant (e.g. instant b in figure 4) to obtain the wavenumber (circles), and compare with the dominant wavenumber by linear stability analysis (red cross, equation (3.10)) in figure 7(b). The dominant wavenumber is that of the maximum exponential growth rate s at a certain Pe . Regarding the fluctuation of E_k , we evaluate the standard deviation of E_k after reaching the statistical steady state in figure 7(c).

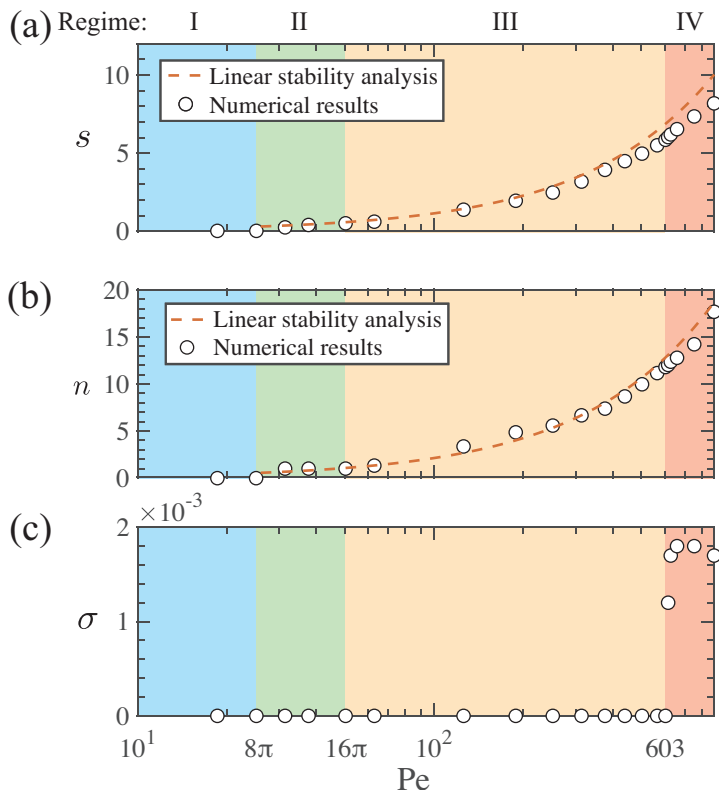


FIGURE 7. The simulation result for the catalytic plane with non-linear terms and random initial perturbation for $Sc = 1$ and different Pe : (a) Theoretical (dashed curve, which is equation (3.9)) and numerical result (circle) of s as a function of Pe , which indicates that the system becomes unstable when $Pe > 8\pi$. (b) Theoretical (dashed line, equation (3.10)) dominant wavenumber and numerical wavenumber n calculated by Fourier transform (circle) as a function of Pe . The result indicates that when $Pe > 16\pi$, multiple plumes are generated. (c) Standard deviation σ of the kinetic energy for different Pe , which indicates that when $Pe \gtrsim 603$, the kinetic energy eventually fluctuates because small plumes are continuously generated. Thus four regimes are classified, marked with different colors: stable (I: blue), a single wave (II: green), multiple waves which merge with each other (III: orange), and multiple waves with small plumes continuously being regenerated (IV: pink).

The four regimes are as follows:

- Regime I ($Pe \leq 8\pi$): the system is stable.
- Regime II ($8\pi < Pe \leq 16\pi$): the system becomes unstable. Single plumes generate as can be seen in figure 7(b), and thus the dominant wavenumber is 1.
- Regime III ($16\pi < Pe \lesssim 603$): the initial wavenumber n becomes larger than one, and it increases with Pe . The trigger of higher-order mode can be explained by the linear stability curve in figure 5. As $Pe > 16\pi$, the perturbation of wavenumber $n > 1$ becomes unstable. For high enough Pe , a higher wavenumber mode can grow even faster than the single wavenumber mode. After a while, the individual plumes merge into a single large one, and the system reaches an asymptotic state with constant E_k ($\sigma = 0$ shown in figure 7(c));
- Regime IV ($Pe \gtrsim 603$): the plume emission and merging happen continuously even after reaching statistical steady state, and therefore E_k fluctuates with time ($\sigma > 0$).

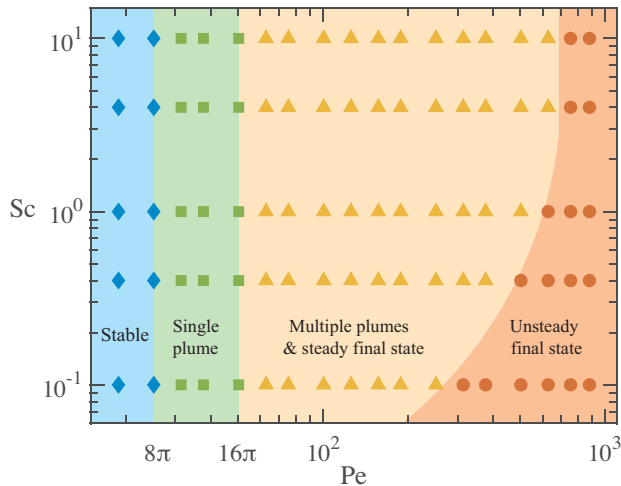


FIGURE 8. The phase diagram for the case of the catalytic plane with different Sc and Pe : For $Pe < 8\pi$, the system is stable; for $8\pi < Pe < 16\pi$, the system becomes unstable and a single plume is generated; finally, for $Pe > 16\pi$, multiple plumes are generated. For the last regime, there are two sub-regimes: for low Pe (orange triangle), multiple plumes eventually merge to a single one and for higher Pe (red circle), there is a newly found regime where the smaller plumes are continuously regenerated. The underlay colors are to guide the eyes.

Figures 7(a) and (b) indicate that the exponential growth rate and the number of plumes generated initially can be approximately predicted by linear stability analysis. However, at high Pe , there is a small deviation between the theory and our simulation. An explanation is that at high Pe , various wavenumbers are excited simultaneously, such that the average growth rate becomes lower than the maximum growth rate predicted by linear stability analysis (equation (3.9)).

Based on the same classification criteria, we work out the phase diagram for the four regimes with five Sc ranging from 0.1 to 10. It is observed that the transition points between stable and unstable regimes ($Pe = 8\pi$), and between the single plume and multiple plumes ($Pe = 16\pi$), are insensitive to Sc . This can be understood from the linear stability analysis where the onset s for n th wavenumber is $Pe = 8\pi n$ which is independent of Sc . However, the onset of regime IV occurs at smaller Pe for smaller Sc . The reason is that less viscosity leads to a more chaotic flow. Therefore plumes emit more frequently in smaller Sc flows.

As a final remark, Michelin *et al.* (2020) have shown the diffusio-phoretic instability in a confined phoretic channel, from which they also observe the generation of the plumes. However, different from their assumption of Stokes flow ($Sc \rightarrow \infty$), we have also considered the cases with various Sc and the non-linear effect. The simultaneous plume emission and merging is one of the unique features of the non-linear simulations, which, however, has been neglected in most of the previous studies using linearized equations.

5. Simulation of the phoretic particle

Given the analysis of the catalytic plane, we now conduct three-dimensional simulations of a spherical phoretic particle to study the effect of plume emission and merging on the particle motion.

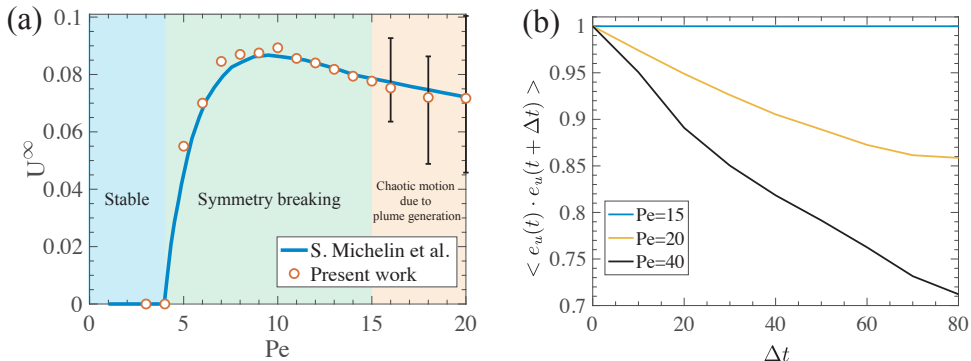


FIGURE 9. (a) The terminal velocity U^∞ of phoretic particles in 3D as function of Pe ($Sc = 1$). The result from the axisymmetric simulation of Michelin *et al.* (2013) is shown as blue solid curve. Our results for the full three-dimensional case are indicated by the red circles. The points for $Pe > 15$ indicate the average terminal velocity. The range of fluctuations is shown by the solid bars, which is based on the maximum deviation. The motion of the phoretic particle is divided into three different regimes: stable, symmetry breaking, and chaotic motion due to plume generation. (b) The temporal auto-correlation function of the unit direction vector for three different Pe ($Sc = 1$). The temporal auto-correlation indicates whether the particle performs chaotic motion or not.

5.1. Numerical setup

The set-up is as follows: a phoretic particle is positioned at the center of the domain, and then due to diffusio-phoresis, the particle will self-propel. The simulation uses the same non-dimensional equations as those in (2.3 - 2.4). It consists of two parts. The first is the same as that in section 4.1, which is to solve the three dimensional version of (2.3 - 2.4), except for the characteristic length which is the radius of the particle. The second part involves the governing equation for the dynamics of the phoretic particle. However, one faces the challenge of dealing with a moving immersed boundary condition. To deal with it, we make use of moving least squares (MLS) based immersed boundary (IB) method, where the particle interface is represented by a triangulated Lagrangian mesh. For details of our MLS-based IB method, we refer to Spandan *et al.* (2017). The concentration boundary condition again is that the wall normal concentration gradient is a constant $\frac{\partial c}{\partial n} = A = 1$, which can be achieved by forcing the concentration at the particle surface based on the concentration interpolated at the probe located at a short distance (1 grid size) from the surface of the particle. The velocity boundary condition is

$$u_s = \nabla_s c, \quad (5.1)$$

where u_s is the surface gradient (∇_s) of the concentration. The domain size is $L_x \times L_y \times L_z = 10R \times 10R \times 20R$, in terms of the particle radius R . We use uniform grids $N_x \times N_y \times N_z = 201 \times 201 \times 401$.

In this case of the spherical particle, the radius R is used as the length scale in Péclet number:

$$Pe = \frac{M|\alpha|R}{D^2}. \quad (5.2)$$

We will present the result of phoretic particles for different Pe from 3 to 20 with Sc fixed at 1.

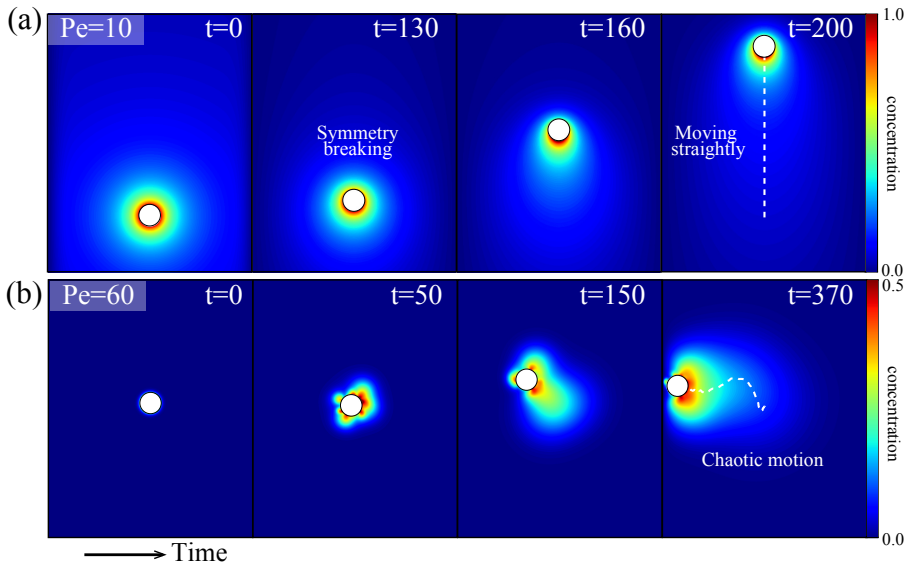


FIGURE 10. The concentration cross-section from three-dimensional simulations of an isotropic catalytic particle for $Pe = 10$ and 60 . Again, $Sc = 1$. The simulation is at a domain $L_x \times L_y \times L_z = 10R \times 10R \times 20R$, in terms of the particle radius R . The grids are $201 \times 201 \times 401$. To better demonstrate the chaotic trajectory, the motion of the particle in (b) is projected to x-z plane. (a) $Pe = 10$, the particle moves straightly. (b) $Pe = 60$, plumes are generated at the surface of the particle, which starts to move irregularly.

5.2. Result of the phoretic particle

Similar to the case of the catalytic plane, the diffusio-phoretic instability breaks the rotational-symmetry of the phoretic particle. It has been shown by [Michelin *et al.* \(2013\)](#) that the phoretic particle breaks the symmetry when Pe is larger than 4. Therefore, as a validation, we first simulate cases with small Pe and compare to the results obtained from [Michelin *et al.* \(2013\)](#). In figure 9 (a), we plot the numerical terminal velocity U^∞ . For $Pe > 4$, indeed symmetry breaking occurs (e.g. figure 10 (a) for $Pe = 10$) and the particle moves along a straight trajectory. The terminal velocity agrees well with those obtained from [Michelin *et al.* \(2013\)](#).

After this validation we now extend the calculations to higher Pe . Multiple plumes emission and merging occur at the surface of the phoretic particle (e.g. figure 10 (b) for $Pe = 60$), which is similar to that observed for the catalytic plane. The continuously emitted plumes change the direction of the phoretic particle and lead to chaotic motion.

To characterize the motion of the particle, we calculate the mean temporal auto-correlation of the particle direction:

$$\langle \mathbf{e}_u(t) \cdot \mathbf{e}_u(t + \Delta t) \rangle = \frac{1}{T} \int_0^T \mathbf{e}_u(t) \cdot \mathbf{e}_u(t + \Delta t) dt, \quad (5.3)$$

where $\mathbf{e}_u(t) = \mathbf{u}(t)/|\mathbf{u}(t)|$ is the unit direction vector of the particle velocity at t . The integral upper limit T is chosen large enough to achieve statistical stationary. The auto-correlation for different Pe is shown in figure 9 (b). When $Pe = 20$, the auto-correlation becomes considerably less than 1 with increasing Δt , which means that the particle starts to meander in different directions. The chaotic behavior of the particle has also been shown by the fluctuation of velocity in figure 9(a), which is represented by the solid bars. Interestingly, for $Pe \gtrsim 15$, the average velocity (the red circle) still lies near the

result by [Michelin *et al.* \(2013\)](#), but for larger Pe , the velocity shows larger fluctuation, i.e. more chaotic behavior.

Thus we can classify the motion for a phoretic particle into three regimes:

- $Pe < 4$, the particle remains stable.
- $4 < Pe \lesssim 15$, symmetry breaking occurs and the particle moves straight.
- $Pe \gtrsim 15$, the particle moves chaotically.

Figure 10 (b) shows that the plumes are continuously generated and merge, which alters the concentration distribution and steer the moving direction of the phoretic particle. This shows that our newly found regime IV in figure 8 leads to the chaotic motion for the case of phoretic particles. It is worth to note that for the case of active droplets, it is also found that the droplets move in a helical or even chaotic trajectory at high Pe ([Maass *et al.* 2016](#); [Suga *et al.* 2018](#); [Vajdi Hokmabad *et al.* 2020](#)). Due to the similarity between diffusio-phoretic and Marangoni effects, a similar mechanism can be the reason behind the active droplet's chaotic motion.

6. Concluding remarks

In summary, we have studied the instability driven by diffusio-phoretic effects at the interfaces for two different systems: a catalytic plane and a spherical phoretic particle. The Péclet number (Pe) and Schmidt number (Sc) are the parameters that determine the states of the system.

For a catalytic plane, via linear stability analysis, we quantitatively studied the growth of various wavenumber perturbation. With assistance of the simulation, we have classified four regimes for different Pe and Sc based on the exponential growth rate of the instability, number of plumes generated initially and fluctuation of the kinetic energy after reaching the statistical steady state (E_k). For $Pe \leq 8\pi$, the system is stable. For $8\pi < Pe \leq 16\pi$, the system becomes unstable, a single plume is generated and the system reaches a steady state eventually. For $Pe > 16\pi$, multiple plumes are generated initially, which merge into a single one to attain a stable state eventually due to non-linear saturation. However, for even higher Pe ($Pe \gtrsim 603$ for $Sc = 1$), small plumes are continuously generated and merge with each other, the system remains unstable and therefore E_k fluctuates in time. The transition to the last regime happens at smaller Pe for smaller Sc due to smaller viscosity compared to diffusivity.

Then we extend our research to three-dimensional simulations of the spherical phoretic particle. Despite the geometric difference, an analogous phenomenon happens at the surface of the particle which triggers different particle motions. Similar to the case of the catalytic plane, for the case at $Sc = 1$, when $Pe > 4$, the particle starts to break the symmetry. For higher $Pe \gtrsim 15$, also similar to the observation of the catalytic plane, the small plumes start to be generated continuously at the surface of the particle, which will steer the particle and lead to meandering motion. The analogous phenomenon indicates that the chaotic motion of the phoretic particle results from the instability at the interface driven by diffusio-phoretic effects.

Many questions remain open. E.g. how does the particle motion and flow field change for phoretic particles in a complicated environment, such as phoretic particle near a wall? How does the plume generation and merging change the collective behavior of phoretic particles? How about the effect of plume generation on rod particles rather than spheres? Building on the here obtained insight into the mechanism behind the chaotic motion of phoretic particles, it is worthwhile to further explore the effects of the plume generation on the motion of particles in the more complicated setups as mentioned above, in particular, on collective effects.

Acknowledgements

We greatly appreciate the valuable discussions with Maziyar Jalaal, Chong Shen Ng, Qi Wang, Babak Vajdi Hokmabad, Corinna Maass and Andrea Prosperetti. We acknowledge the support from the Netherlands Center for Multiscale Catalytic Energy Conversion (MCEC), an NWO Gravitation program funded by the Ministry of Education. We acknowledge that the results of this research have been achieved using the DECI resource Kay based in Ireland at Irish HPC center with support from the PRACE. We also acknowledge PRACE for awarding us access to MareNostrum at the Barcelona Supercomputing Centre (BSC) under PRACE project number 2017174146 and JUWELS at the Jülich Supercomputing Centre. This work was also partly carried out on the national infrastructure of SURFsara with the support of SURF Cooperative, the collaborative ICT organization for Dutch education and research.

Declaration of interests

The authors report no conflict of interest.

REFERENCES

- ANDERSON, J. L. 1989 Colloid transport by interfacial forces. *Annu. Rev. Fluid Mech.* **21** (1), 61–99.
- BÄR, M., GROSSMANN, R., HEIDENREICH, S. & PERUANI, F. 2020 Self-propelled rods: Insights and perspectives for active matter. *Annu. Rev. Condens. Matter Phys.* **11**, 441–466.
- BRAY, D. 2000 *Cell movements: from molecules to motility*. Garland Science.
- EBBENS, S. J. & HOWSE, J. R. 2010 In pursuit of propulsion at the nanoscale. *Soft Matter* **6** (4), 726–738.
- GOLESTANIAN, R., LIVERPOOL, T. B. & AJDARI, A. 2007 Designing phoretic micro- and nanoswimmers. *New J. Phys.* **9** (5), 126.
- GREENSIDE, H. S. & COUGHRAN JR, W. M. 1984 Nonlinear pattern formation near the onset of Rayleigh-Bénard convection. *Phys. Rev. A* **30** (1), 398.
- GROSSMANN, S., LOHSE, D. & SUN, C. 2016 High Reynolds number Taylor-Couette turbulence. *Annu. Rev. Fluid Mech.* **48** (1), 53–80.
- HAAN, S. W. 1989 Onset of nonlinear saturation for Rayleigh-Taylor growth in the presence of a full spectrum of modes. *Phys. Rev. A* **39** (11), 5812.
- HERMINGHAUS, S., MAASS, C. C., KRÜGER, C., THUTUPALLI, S., GOEHRING, L. & BAHR, C. 2014 Interfacial mechanisms in active emulsions. *Soft matter* **10** (36), 7008–7022.
- HU, W., LIN, T., RAFAI, S. & MISBAH, C. 2019 Chaotic swimming of phoretic particles. *Phys. Rev. Lett.* **123**, 238004.
- JEANNERET, R., PUSHKIN, D. O., KANTSLER, V. & POLIN, M. 2016 Entrainment dominates the interaction of microalgae with micron-sized objects. *Nat. Commun.* **7** (1), 1–7.
- JIANG, S., CHEN, Q., TRIPATHY, M., LUIJTEN, E., SCHWEIZER, K. S. & GRANICK, S. 2010 Janus particle synthesis and assembly. *Adv. Mater.* **22** (10), 1060–1071.
- JIN, C., KRÜGER, C. & MAASS, C. C. 2017 Chemotaxis and autochemotaxis of self-propelling droplet swimmers. *Proc. N. Acad. Sci.* **114** (20), 5089–5094.
- KRÜGER, C., KLÖS, G., BAHR, C. & MAASS, C. 2016 Curling liquid crystal microswimmers: A cascade of spontaneous symmetry breaking. *Phys. Rev. Lett.* **117** (4), 048003.
- LAUGA, E. 2016 Bacterial hydrodynamics. *Annu. Rev. Fluid Mech.* **48**, 105–130.
- LAUGA, E. & THOMAS, R. P. 2009 The hydrodynamics of swimming microorganisms. *Rep. Prog. Phys.* **72** (9), 096601.
- LI, Y., DIDDENS, C., PROSPERETTI, A., CHONG, K. L., ZHANG, X. & LOHSE, D. 2019 Bouncing oil droplet in a stratified liquid and its sudden death. *Phys. Rev. Lett.* **122** (15), 154502.
- LOHSE, D. & ZHANG, X. 2020 Physicochemical hydrodynamics of droplets out of equilibrium, arXiv: 2005.03782.

- LONG, D., STONE, H. A. & AJDARI, A. 1999 Electroosmotic flows created by surface defects in capillary electrophoresis. *J. Colloid. Interf. Sci.* **212** (2), 338–349.
- MAASS, C. C., KRÜGER, C., HERMINGHAUS, S. & BAHR, C. 2016 Swimming droplets. *Annu. Rev. Condens. Matter Phys.* **7**, 171–193.
- MICHELIN, S., GAME, S., LAUGA, E., KEAVENY, E. & PAPAGEORGIOU, D. 2020 Spontaneous onset of convection in a uniform phoretic channel. *Soft Matter* **16**, 1259–1269.
- MICHELIN, S. & LAUGA, E. 2014 Phoretic self-propulsion at finite Péclet numbers. *J. Fluid Mech.* **747**, 572–604.
- MICHELIN, S., LAUGA, E. & BARTOLO, D. 2013 Spontaneous autophoretic motion of isotropic particles. *Phys. Fluids* **25** (6), 061701.
- MORAN, J. L. & POSNER, J. D. 2011 Electrokinetic locomotion due to reaction-induced charge auto-electrophoresis. *J. Fluid Mech.* **680**, 31–66.
- MORAN, J. L. & POSNER, J. D. 2017 Phoretic self-propulsion. *Annu. Rev. Fluid Mech.* **49**, 511–540.
- MOROZOV, M. & MICHELIN, S. 2019 Nonlinear dynamics of a chemically-active drop: From steady to chaotic self-propulsion. *J. Chem. Phys.* **150** (4), 044110.
- PIAZZA, R. 2008 Thermophoresis: moving particles with thermal gradients. *Soft Matter* **4** (9), 1740–1744.
- VAN DER POEL, E. P., OSTILLA-MÓNICO, R., DONNERS, J. & VERZICCO, R. 2015 A pencil distributed finite difference code for strongly turbulent wall-bounded flows. *Comput. Fluids* **116**, 10–16.
- QI, K., WESTPHAL, E., GOMPPER, G. & WINKLER, R. G. 2020 Enhanced rotational motion of spherical squirmer in polymer solutions. *Phys. Rev. Lett.* **124**, 068001.
- RAMASWAMY, S. 2010 The mechanics and statistics of active matter. *Annu. Rev. Condens. Matter Phys.* **1** (1), 323–345.
- RUCKENSTEIN, E. 1981 Can phoretic motions be treated as interfacial tension gradient driven phenomena? *J. Colloid. Interf. Sci.* **83** (1), 77–81.
- SPANDAN, V., MESCHINI, V., OSTILLA-MÓNICO, R., LOHSE, D., QUERZOLI, G., DE TULLIO, M. D. & VERZICCO, R. 2017 A parallel interaction potential approach coupled with the immersed boundary method for fully resolved simulations of deformable interfaces and membranes. *J. Comput. Phys.* **348**, 567–590.
- SQUIRES, T. M. & BAZANT, M. Z. 2006 Breaking symmetries in induced-charge electro-osmosis and electrophoresis. *J. Fluid Mech.* **560**, 65–101.
- SUGA, M., S., SUDA, ICHIKAWA, M. & KIMURA, Y. 2018 Self-propelled motion switching in nematic liquid crystal droplets in aqueous surfactant solutions. *Phys. Rev. E* **97** (6), 062703.
- VAJDI HOKMABAD, B., BALDWIN, K. A., KRÜGER, C., BAHR, C. & MAASS, C. C. 2019 Topological stabilization and dynamics of self-propelling nematic shells. *Phys. Rev. Lett.* **123**, 178003.
- VAJDI HOKMABAD, B., DEY, R., JALAAL, M., MOHANTY, D., ALMUKAMBETOVA, M., BALDWIN, K. A., LOHSE, D. & MAASS, C. C. 2020 Stop-and-go droplet swimmers, arXiv: 2005.12721.
- VERZICCO, R. & ORLANDI, P. 1996 A finite-difference scheme for three-dimensional incompressible flows in cylindrical coordinates. *J. Comput. Phys.* **123** (2), 402–414.
- WU, J. Z., MA, H. Y. & ZHOU, M. D. 2006 *Vorticity and Vortex Dynamics*. Berlin: Springer.